AIAA JOURNAL
Vol. 44, No. 8, August 2006

Aerodynamic Shape Optimization of Hovering Rotor Blades in Transonic Flow Using Unstructured Meshes

Sang Wook Lee* and Oh Joon Kwon†
Korea Advanced Institute of Science and Technology, Daejeon 305-701, Republic of Korea

DOI: 10.2514/1.15385

An aerodynamic shape optimization technique has been developed for helicopter rotor blades in hover based on a continuous adjoint method on unstructured meshes. For this purpose, the Euler flow solver and the adjoint sensitivity analysis were formulated on the rotating frame of reference. To handle the repeated evaluation of the flow solution and the sensitivity analysis efficiently, the flow and adjoint solvers were parallelized using a domain decomposition strategy. A solution-adaptive mesh refinement technique was adopted to better resolve the tip vortex. Applications were made to the aerodynamic shape optimization of the Caradonna–Tung rotor blade and the UH-60 rotor blade. The results showed that the present method is effective in determining optimum aerodynamic configurations of rotor blades in hover, which require minimum inviscid torque while maintaining the desired thrust level at transonic flight conditions.

Nomenclature

$\boldsymbol{d}$	=	vector of design variables
e_o	=	total internal energy
g	=	arbitrary function of flow variables
h_o	=	total enthalty
I	=	objective function of unconstraint optimization
I_o	=	objective function of constraint optimization
k	=	arbitrary function of design variables
n	=	design iteration
ndv	=	number of design variables
p	=	static pressure
$\boldsymbol{Q}$	=	vector of flow variables
$\boldsymbol{R}$	=	residual vector of governing flow equations
R	=	rotor radius
r	=	radial distance along blade span
$\boldsymbol{s}$	=	vector of search direction
U	=	inertial velocity component normal to domain boundary
u, v, w	=	Cartesian velocity components in inertial frame of reference
δ	=	variation operator
ϵ	=	arbitrary small number
λ	=	step size
ρ	=	flow density
$\boldsymbol{\Psi}$	=	vector of adjoint variables

Subscript

L	=	left side of control surface
R	=	right side of control surface

Introduction

AERODYNAMIC shape optimization is one of the most important research areas in current computational fluid dynamics, enabling aircraft designers to determine optimum aerodynamic configurations. In the early days of development, its application was mostly restricted to simple two-dimensional geometries due to the lack of sufficient computational power. However, recent advancement in computer hardware technology and numerical algorithms made possible its application to more complex three-dimensional configurations. Presently, several variations of aerodynamic shape optimization techniques are available. One of the most popular methods is the gradient-based optimization technique in which sensitivities, the gradients of objective function with respect to design variables, are used to update the design variables in the direction that a specified objective function is minimized in a systematic way.

Several research works were previously conducted for the efficient evaluation of the sensitivities. The classical finite-difference method determines the gradients by taking the difference of the objective function values obtained by perturbing the design variables. Even though this method is easy to apply, it requires multiple flow solutions, at least equal to the number of design variables. Thus its application to three-dimensional configurations is very impractical. Recently, particular interest has been given to adjoint methods, in which sensitivities are calculated indirectly from single evaluation of the flow and adjoint equations [1]. Because the computational time for solving the adjoint equations is similar to that for solving the flow equations, independent of the number of design variables, adjoint methods are widely used for the aerodynamic shape optimization of three-dimensional configurations requiring a large number of design variables [2–5].

Shock waves in transonic flow not only increase the wave drag but also cause unfavorable flutter or buffet to fixed wings. Helicopter rotor blades in forward flight are also frequently exposed to strong unsteady shock waves at the blade tip region. These shock waves increase the required torque and become a source of undesirable noise and vibration. Thus elimination of these shock waves or possible reduction of their strength is desirable for the enhancement of the performance of helicopters. However, application of the aerodynamic shape optimization techniques has been mostly limited to fixed-wing configurations, and the aerodynamic design of helicopter rotor blades has not benefitted much by the current optimization techniques. Because the flow field of rotor blades is very complex, inherently unsteady, and highly three dimensional, the application of aerodynamic design optimization techniques to rotor blades is much more challenging than to fixed wings.

Currently, a limited number of previous research works on the aerodynamic shape optimization of helicopter rotor blades are available. Tapia et al. [6] developed an inverse design method for rotor blades based on a full-potential flow analysis. From the prescribed target pressure distributions, blade section contours at a

Received 4 January 2005; revision received 23 January 2006; accepted for publication 24 January 2006.

*Graduate Research Assistant, Department of Aerospace Engineering.
†Professor, Department of Aerospace Engineering, 373-1 Guseong-dong, Yuseong-gu; ojkwon@kaist.ac.kr. Senior Member AIAA. Corresponding author.

few spanwise control stations were designed in forward flight using a multipoint design technique. Fanjoy and Crossley [7] applied a genetic algorithm to the two-dimensional airfoil section design of helicopter rotor blades based on a panel method. Sun et al. [8] performed a study about the geometric parameter optimization of helicopter rotor blades in forward flight using a response surface method coupled with a genetic algorithm based on a free-wake panel method. The response surface method requires one to evaluate the flow solution many times, and thus the application to high fidelity flows in three dimensions is impractical.

In the present study, an aerodynamic shape optimization technique for helicopter rotor blades in hover has been developed based on a continuous adjoint method and the Euler flow analysis on unstructured meshes. For the efficient evaluation of the sensitivities, the adjoint analysis and the flow solver were formulated on the rotating frame of reference [9]. The blade section contour was represented by using the Hicks–Henne shape functions [10]. Mesh movement due to the changing blade geometry was handled by using a spring analogy [11]. A solution-adaptive mesh refinement method was adopted to better resolve the tip vortex [12]. To handle the large computational time involved in the repeated evaluation of the flow and adjoint solvers, a parallel computation algorithm based on domain decomposition was adopted [13]. Calculations were made for a single rotor blade by applying a periodic boundary condition between blades. Validations were made for the Caradonna–Tung experimental rotor blade [14] and the UH-60 rotor blade [15] in hover.

Numerical Method

Flow Solution

The equations governing three-dimensional, inviscid, compressible flows are the Euler equations, which can be recast for absolute flow variables on a rotational frame of reference. The equations may be written in an integral form for a bounded domain V with a boundary ∂V:

$$\frac{\partial}{\partial t}\int_V \boldsymbol{Q}\,\mathrm{d}V + \oint_{\partial V} \mathbf{F}(\boldsymbol{Q},\boldsymbol{n})\,\mathrm{d}S = \int_V \mathbf{S}\,\mathrm{d}V \tag{1}$$

where

$$\boldsymbol{Q} = \begin{pmatrix} \rho \\ \rho u \\ \rho v \\ \rho w \\ e_o \end{pmatrix}, \qquad \mathbf{F}(\boldsymbol{Q},\boldsymbol{n}) = \begin{pmatrix} \rho U_r \\ \rho u U_r + p n_x \\ \rho v U_r + p n_y \\ \rho w U_r + p n_z \\ e_o U_r + p U \end{pmatrix},$$
$$\mathbf{S} = \Omega \begin{pmatrix} 0 \\ \rho v \\ -\rho u \\ 0 \\ 0 \end{pmatrix} \tag{2}$$

Here, Ω is the rotor angular velocity relative to the inertial frame, and n_x, n_y, and n_z are the Cartesian components of the exterior surface unit normal vector $\boldsymbol{n}$ on the boundary ∂V. U_r is the component of the relative velocity normal to the domain boundary.

The governing flow equations are discretized based on a cell-based finite-volume method. The inviscid flux across each cell face is computed using Roe's flux-difference splitting scheme. To obtain second-order spatial accuracy, estimation of the state variables at each cell face is achieved by interpolating the solution using the Taylor series expansion in the neighborhood of each cell center. The cell-averaged solution gradient required at the cell center for the above expansion is computed from Gauss's theorem by evaluating the surface integral for the closed surface of the tetrahedra [16]. An implicit time integration algorithm based on the linearized Euler backward differencing is used to advance the solution in time. At each time step the linear system of equations is solved using a point Gauss–Seidel method.

On the solid surface of the rotor blade, the flow tangency condition is applied. The grid velocity due to rotation is also accounted for at the solid surface. At the far-field boundary, a source-sink boundary condition proposed by Srinivasan et al. [17] is used. Because of the periodic nature of the flow of hovering rotors, calculations are made for a single blade and the periodic boundary condition is imposed between blades.

Sensitivity Analysis

The aerodynamic shape optimization problem of rotor blades may be expressed as

$$\text{minimize } I_o(\boldsymbol{Q},\boldsymbol{d}) \qquad \text{subject to } \boldsymbol{R}(\boldsymbol{Q},\boldsymbol{d}) = 0 \tag{3}$$

The objective function $I_o(\boldsymbol{Q},\boldsymbol{d})$ is the integration of the distributed pressure over the blade surface:

$$I_o = \oint_{\partial V} g(\boldsymbol{Q}(\boldsymbol{d}))k(\boldsymbol{d})\,\mathrm{d}S \tag{4}$$

where $g(\boldsymbol{Q}(\boldsymbol{d}))$ and $k(\boldsymbol{d})$ are the functions of flow variables and design variables, respectively. The constraint function $\boldsymbol{R}(\boldsymbol{Q},\boldsymbol{d})$ is the residual of the governing flow equations as described in Eq. (1).

Because this nonlinear constraint minimization problem requires a relatively large calculation time, it is recast to an unconstraint optimization problem by introducing the Lagrangian multipliers known as the adjoint variables. Then the new objective function can be defined as

$$I(\boldsymbol{Q},\boldsymbol{d},\boldsymbol{\Psi}) = I_o(\boldsymbol{Q},\boldsymbol{d}) + \boldsymbol{\Psi}^T\boldsymbol{R}(\boldsymbol{Q},\boldsymbol{d}) \tag{5}$$

where $\boldsymbol{\Psi}$ is the vector of the adjoint variables.

The adjoint equations of the Euler equations are obtained by taking the variation of Eq. (5) with respect to the design variables and regrouping terms [9]:

$$\frac{\partial}{\partial t}\int_V \boldsymbol{\Psi}\,\mathrm{d}V - \oint_{\partial V} \boldsymbol{G}(\boldsymbol{\Psi},\boldsymbol{Q},\boldsymbol{n})\,\mathrm{d}S = \int_V \mathbf{D}^T\boldsymbol{\Psi}\,\mathrm{d}V \tag{6}$$

Here $\boldsymbol{G}(\boldsymbol{\Psi},\boldsymbol{Q},\boldsymbol{n})$ represents the adjoint flux vector defined as

$$\boldsymbol{G}(\boldsymbol{\Psi},\boldsymbol{Q},\boldsymbol{n}) = \left(\frac{\partial \mathbf{F}(\boldsymbol{Q},\boldsymbol{n})}{\partial \boldsymbol{Q}}\right)^T \boldsymbol{\Psi} \tag{7}$$

$\mathbf{D}$ is the Jacobian matrix of the source term $\mathbf{S}$ of Eq. (1) added due to rotor rotation. The corresponding adjoint boundary condition at the solid surface can be expressed as

$$\Psi_2 n_x + \Psi_3 n_y + \Psi_4 n_z + \Psi_5\theta + k\frac{\partial g}{\partial p} = 0 \tag{8}$$

where the contribution of rotor rotation is included in the contravariant velocity θ.

The adjoint sensitivity is obtained by

$$\delta I = \oint_{\partial V} g\,\delta k\,\mathrm{d}S - \oint_{\partial V} \eta\Lambda\,\mathrm{d}S \tag{9}$$

where η and Λ can be written as

$$\eta = (\Psi_1 + u\Psi_2 + v\Psi_3 + w\Psi_4 + h_o\Psi_5) \tag{10}$$

$$\Lambda = \delta x\left(\frac{\partial u}{\partial x}n_x + \frac{\partial v}{\partial x}n_y + \frac{\partial w}{\partial x}n_z\right) + \delta y\left(\frac{\partial u}{\partial y}n_x + \frac{\partial v}{\partial y}n_y + \frac{\partial w}{\partial y}n_z\right) + \delta z\left(\frac{\partial u}{\partial z}n_x + \frac{\partial v}{\partial z}n_y + \frac{\partial w}{\partial z}n_z\right) + (u\delta n_x + v\delta n_y + w\delta n_z) + \delta k_t \tag{11}$$

Here δk_t represents the sensitivity of the grid velocity due to the change of the blade surface shape. The mesh sensitivities of the node and the surface normal vector in x direction can be obtained by taking

a finite difference of the metric terms for a small variation of the design variables:

$$\delta x = \frac{x(\boldsymbol{d}+\epsilon) - x(\boldsymbol{d})}{\epsilon} \qquad \delta n_x = \frac{n_x(\boldsymbol{d}+\epsilon) - n_x(\boldsymbol{d})}{\epsilon} \tag{12}$$

The mesh sensitivities in the other two directions can also be obtained in a similar manner. The computational overhead for evaluating these mesh sensitivities is relatively small, unless the number of design variables becomes excessively large.

In principle, the linear adjoint equations in Eq. (6) can be discretized using any stable method. However, to evaluate the sensitivities accurately, this discretization must be consistent with that of the flow equations. In the present study, the adjoint equations are discretized using a cell-based finite-volume method, similar to that used for the flow equations. The adjoint flux across each cell face f surrounding control volume i is calculated using a second-order accurate upwind scheme [18]:

$$\boldsymbol{G}_f = \frac{1}{2}\left[\boldsymbol{G}(\boldsymbol{\Psi}_i, \boldsymbol{Q}_L, \boldsymbol{n}_f) + \boldsymbol{G}(\boldsymbol{\Psi}_i, \boldsymbol{Q}_R, \boldsymbol{n}_f) + \left(\frac{\partial \Phi}{\partial \boldsymbol{Q}_L}\right)^T (\boldsymbol{\Psi}_R - \boldsymbol{\Psi}_L)\right] \tag{13}$$

where $\Phi = |\tilde{\mathbf{A}}|(\boldsymbol{Q}_R - \boldsymbol{Q}_L)$ and $|\tilde{\mathbf{A}}|$ is the Roe-averaged matrix.

Because the mathematical characteristics of the adjoint equations are identical to those of the flow equations, most of the subroutines developed for the flow solver can be used for solving the adjoint equations with little modification.

Shape Function and Mesh Deformation

During the aerodynamic shape optimization process, the blade geometry changes continuously by following the sensitivity information. Ideally, every node on the blade surface can be used as the design variable. However, practical limitations exist because of the large calculation time for evaluating the mesh sensitivities. Thus proper surface parameterization must be used [2]. In the present study, the Hicks–Henne shape functions [10] were used to reduce the number of design variables and to represent the blade section contours smoothly. The Hicks–Henne shape functions are composed of exponential and sine bumps and are proven to be effective in achieving design improvement, even using a limited number of design variables. The blade geometry can be represented as

$$z = z_o + \sum_{i=1}^{\text{ndv}} \boldsymbol{d}_i f_i \tag{14}$$

where z, z_o, and f_i represent the new coordinate after design, the original geometry, and the shape function, respectively.

Initially, the design variables are set to zero. After each design iteration, the design variables are updated as

$$\boldsymbol{d}^{n+1} = \boldsymbol{d}^n + \lambda \boldsymbol{s}^n \tag{15}$$

where λ is the step size and the vector $\boldsymbol{s}$ is directly determined from the adjoint sensitivity analysis based on a steepest descent algorithm.

During the design iteration, the computational mesh needs to deform to reflect the change in blade surface contour. In the present study, this mesh movement is achieved by satisfying the static force equilibrium based on a spring analogy [11]:

$$\sum_{j=1}^{\kappa} \alpha_{i,j}(\delta_j - \delta_i) = 0 \tag{16}$$

Here δ_i and δ_j represent the coordinate changes of nodes i and j from the given mesh, and κ is the number of neighboring nodes. The spring constant $\alpha_{i,j}$ is assumed to be the inverse of the edge length connecting nodes i and j.

Objective Function

Because the main objective of the present study is to obtain a rotor blade configuration which minimizes the required inviscid torque under the constraint of maintaining the desired thrust level, the objective function is selected as a combination of the thrust and torque coefficients:

$$I_o = w_1(C_{T\,\text{desired}} - C_T)^2 + w_2 C_Q^2 \tag{17}$$

Here w_1 and w_2 are the weighting or penalty coefficients given by the designer by considering the particular design case of interest. When w_1 is much larger than w_2, the thrust after design matches the desired level very closely, whereas the reduction in torque becomes less. On the other hand, if the design objective is a large reduction of torque allowing some variance in thrust, w_2 must be larger than w_1. However, a large difference between the two weighting coefficients increases the stiffness of the design problem, and the design process may fail as a result. In the present study, w_1 and w_2 were set to $1/2$ and $5/2$, respectively.

Solution-Adaptive Mesh Refinement

The aerodynamic performance of helicopter rotor blades in hover is strongly affected by their own wake lingering underneath the rotor disk plane. To preserve the tip vortex and to reflect its effect on the present blade shape optimization accurately, a multilevel solution-adaptive mesh refinement technique [12] was adopted.

At first, the location of local vorticity maximum is searched at

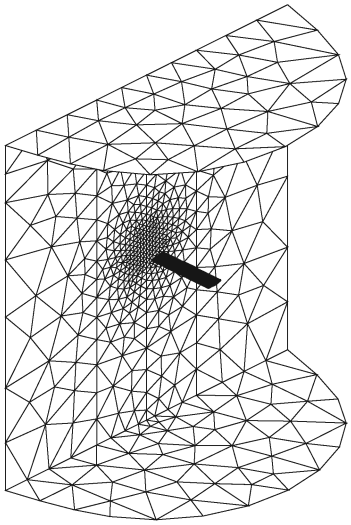

a) Surface triangulations at the computational boundary

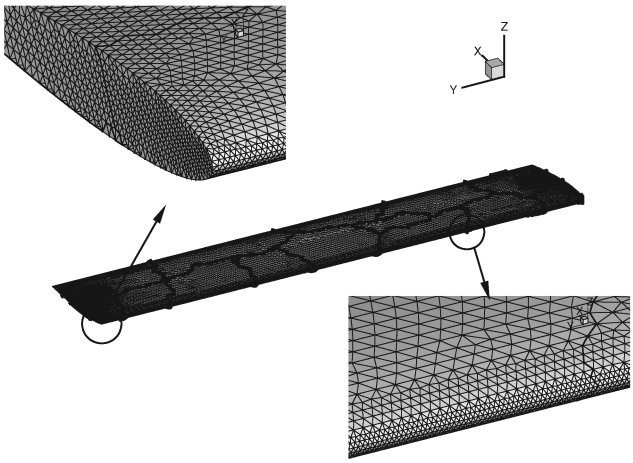

b) Surface triangulations on the rotor blade

Fig. 1 Surface triangulations of the Caradonna–Tung rotor blade.

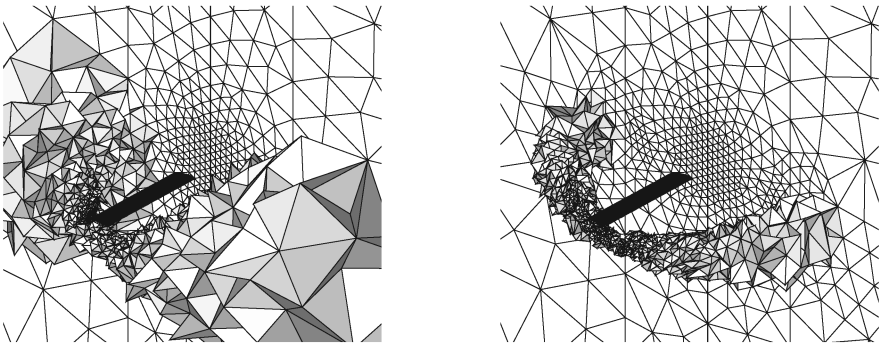

a) First level adaptation: 342,867 cells and 63,088 nodes

b) Second level adaptation: 436,776 cells and 79,143 nodes

c) Third level adaptation: 527,300 cells and 94,710 nodes

d) Fourth level adaptation: 553,943 cells and 99,424 nodes

e) Fifth level adaptation: 563,073 cells and 101,014 nodes

Fig. 2 Wake mesh adaptation sequence for the Caradonna–Tung rotor.

every 5 deg of vortex age from the blade trailing edge. This search continues until the tip vortex core cannot be identified due to numerical dissipation. Next, a smooth line connecting the discrete vortex cores is obtained from a three-dimensional parabolic blending. Then 1:8 division is applied to cells on and near the captured core trajectory by inserting new nodes in the middle of the tetrahedral cell edges. Buffer cells are also inserted between the divided cells and the surrounding cells to confirm a valid cell connectivity. These buffer cells are divided using either a 1:4 or 1:2 division pattern. Then the flow calculation resumes on the refined mesh. This process can be repeated multiple times as necessary.

Parallel Implementation

To reduce the large computational time involved in the repeated evaluation of the flow and adjoint solvers, a parallel algorithm based on a domain decomposition strategy was applied to both solvers. The load balancing between processors was achieved by partitioning the global computational domain into local subdomains using the MeTiS libraries [13]. The message passing interface was used to transfer the flow and adjoint variables across the subdomain boundary. No attempt was made to parallelize the optimization algorithm because this portion is computationally negligible compared with the other elements of the design process.

All calculations were made on a Linux-based PC cluster having 2.4 GHz CPUs.

Results and Discussion

Caradonna–Tung Rotor Blade

At first, the present method was applied to the Caradonna–Tung experimental rotor configuration [14]. The rotor has two untwisted blades, which are made of an NACA0012 airfoil section and have a rectangular planform shape with an aspect ratio of 6. The blade

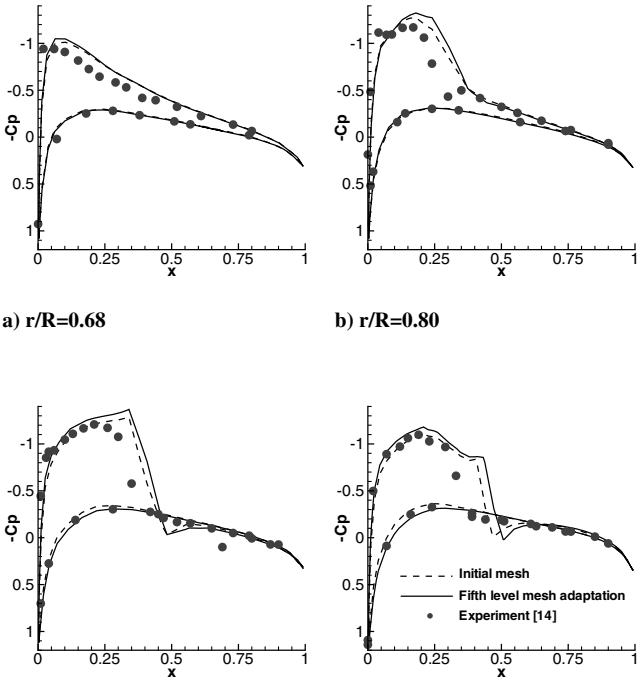

a) r/R=0.68 b) r/R=0.80

c) r/R=0.89 d) r/R=0.96

Fig. 3 Comparison of surface pressure distributions of the Caradonna–Tung rotor blade at a tip Mach number of 0.877 and a blade collective pitch angle of 8 deg.

precone angle is set to 0.5 deg. The rotor adopted for the present study operates at a collective pitch angle of 8 deg and a transonic tip Mach number of 0.877.

Figure 1a shows the surface triangulations at the periodic boundary and at the far-field boundary located two radii away in all directions. The computational domain was initially divided by 314,417 tetrahedral cells and 58,169 nodes. The surface triangulations on the rotor blade are shown in Fig. 1b. The bold lines represent the parallel subdomain boundaries.

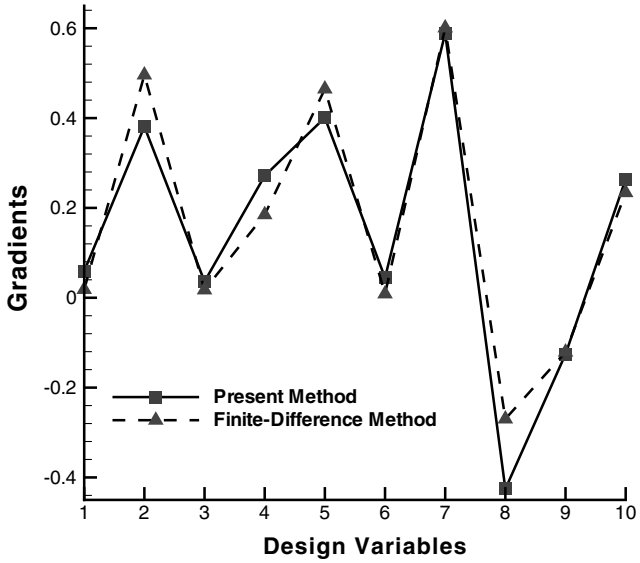

Fig. 4 Comparison of torque sensitivities for the optimization of the Caradonna–Tung rotor blade at a tip Mach number of 0.877 and a blade collective pitch angle of 8 deg.

To reduce the numerical dissipation and to preserve the tip vortex more accurately, five levels of mesh adaptation were applied to the wake as shown in Fig. 2. The cells tagged for refinement along the tip vortex trajectory were divided until the characteristic length of the cell became less than 5% of the blade chord. The final mesh consisted of 563,073 cells and 101,014 nodes. After each level of mesh adaptation, the refined mesh was repartitioned for load balancing.

Initially, the present flow solver was validated by comparing the predicted surface pressure distributions with the experiment [14] at four spanwise stations of the original rotor blade. The results presented in Fig. 3 show that the agreement with the experiment is comparable to other methods [17,19] at all spanwise stations. The figure also shows that the blade loading after the application of wake mesh adaptation increased slightly, particulary at the spanwise stations near the blade tip. This is due to the higher effective angle of attack induced by the interaction between the current blade and the

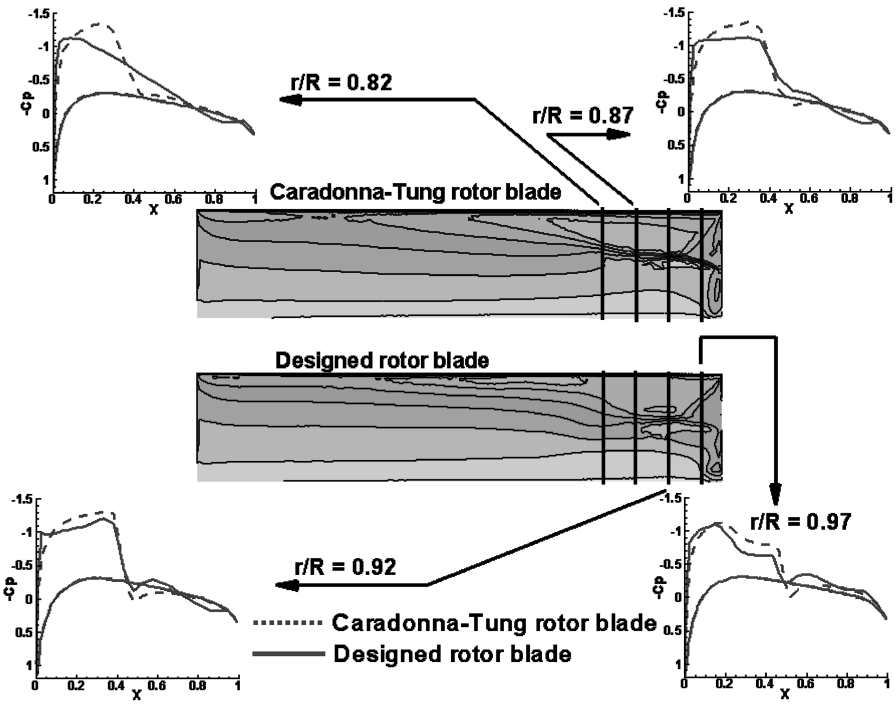

Fig. 5 Comparison of surface pressure distributions of the Caradonna–Tung rotor blade before and after design at a tip Mach number of 0.877 and a blade collective pitch angle of 8 deg.

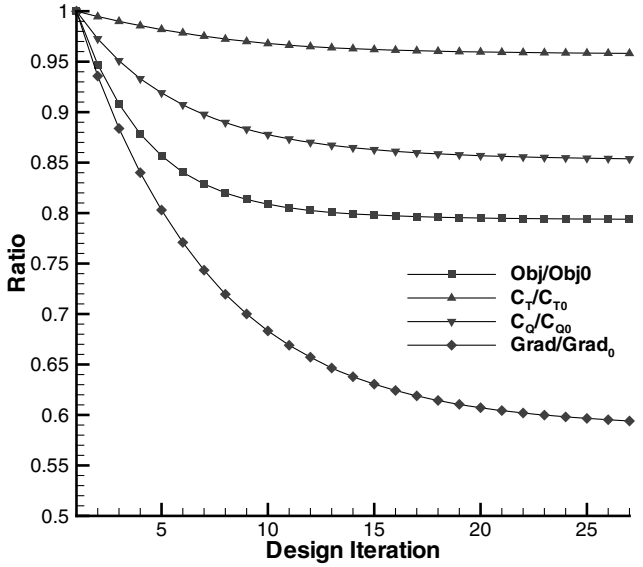

Fig. 6 Design convergence history of the Caradonna–Tung rotor blade.

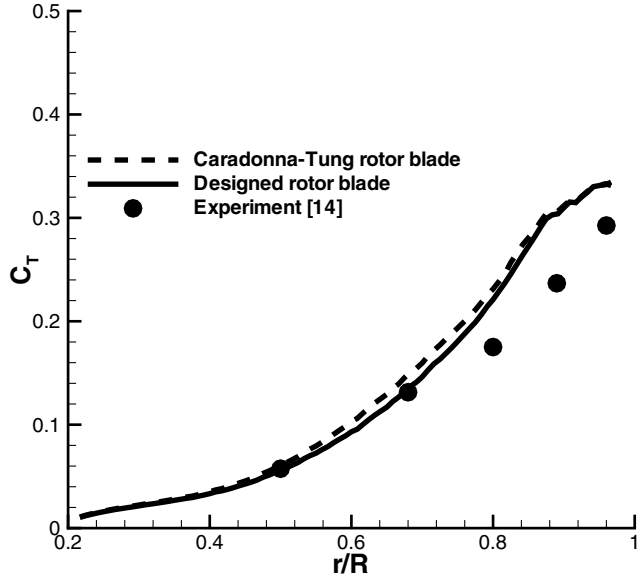

Fig. 7 Comparison of spanwise sectional thrust distributions.

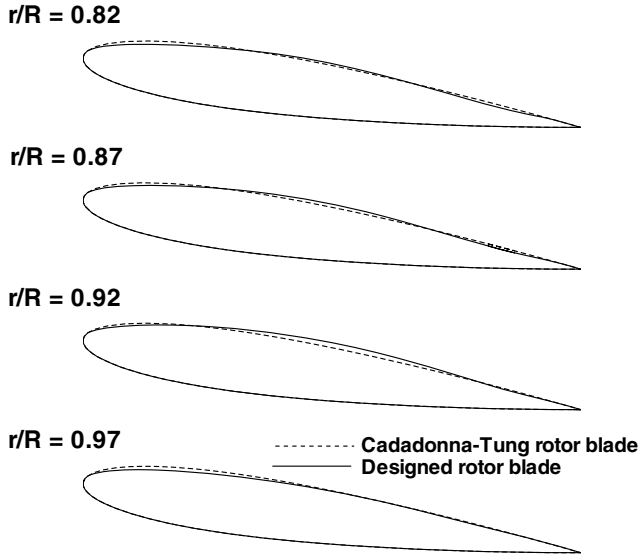

Fig. 8 Comparison of blade section contours of the Caradonna–Tung rotor blade before and after design.

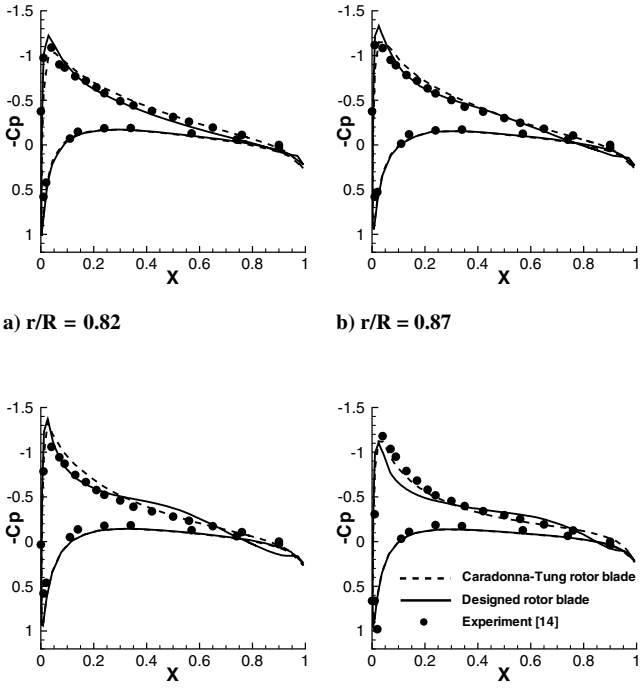

Fig. 9 Comparison of surface pressure distributions of the Caradonna–Tung rotor blade at an off-design subsonic tip Mach number of 0.439 and a blade collective pitch angle of 8 deg.

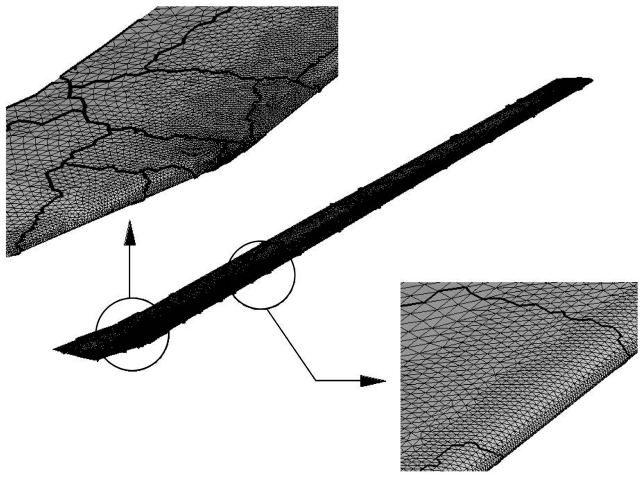

Fig. 10 Surface triangulations of the UH-60 rotor blade.

tip vortex from the preceding blade. The discrepancy between the calculation and the experiment is due to the lack of viscosity of the present method.

Before the actual application of the present shape optimization technique, the accuracy and the efficiency of the present sensitivity analysis method were tested by evaluating the adjoint sensitivities of the rotor torque and comparing the results with those obtained from the finite-difference method. In this test two spanwise stations ($r/R = 0.8,\ 0.9$) were selected as the design sections, and five Hicks–Henne shape functions were adopted on the upper surface for each section. As shown in Fig. 4, sensitivities from both methods are in good agreement, demonstrating the accuracy of the present adjoint method. However, to obtain these results, the finite-difference method required 11 evaluations of the flow solution whereas only one flow solution and one adjoint solution were needed for the present adjoint method. The calculation time by the present method and the finite-difference method was 2240 and 22,140 s, respectively.

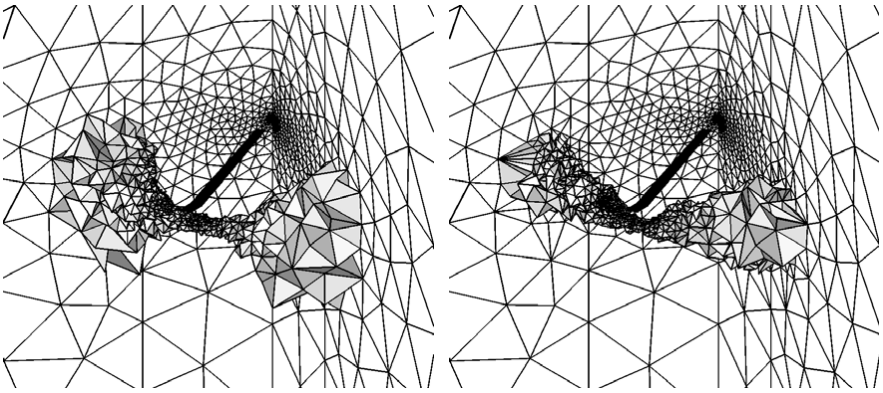

a) First level adaptation: 714,460 cells and 134,744 nodes

b) Second level adaptation: 758,220 cells and 142,293 nodes

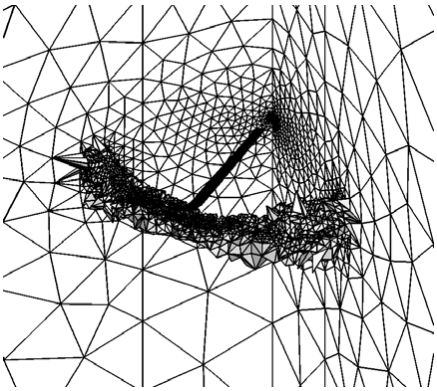

c) Third level adaptation: 823,043 cells and 153,488 nodes

Fig. 11 Wake mesh adaptation sequence for the UH-60 rotor.

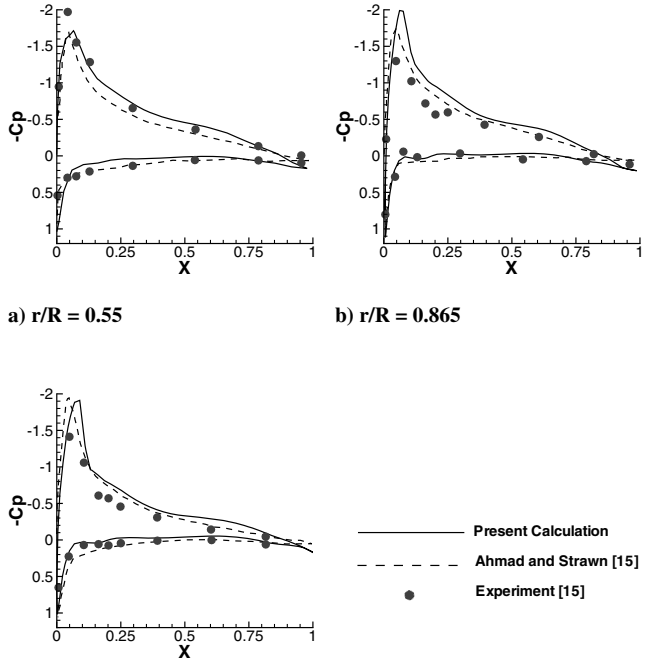

a) r/R = 0.55

b) r/R = 0.865

c) r/R = 0.965

Fig. 12 Comparison of surface pressure distributions of the UH-60 rotor blade at a tip Mach number of 0.628 and a blade collecive pitch angle of 10.47 deg.

Next, the present method was applied to the aerodynamic shape optimization of the blade upper surface on the refined mesh obtained after five levels of mesh adaption. In this application, nine spanwise stations were selected as the design sections ($r/R = 0.65, 0.70, 0.75, 0.80, 0.85, 0.90, 0.93, 0.95, 0.98$) and 10 Hicks–Henne shape functions were adopted at each section, resulting in 90 design variables in total.

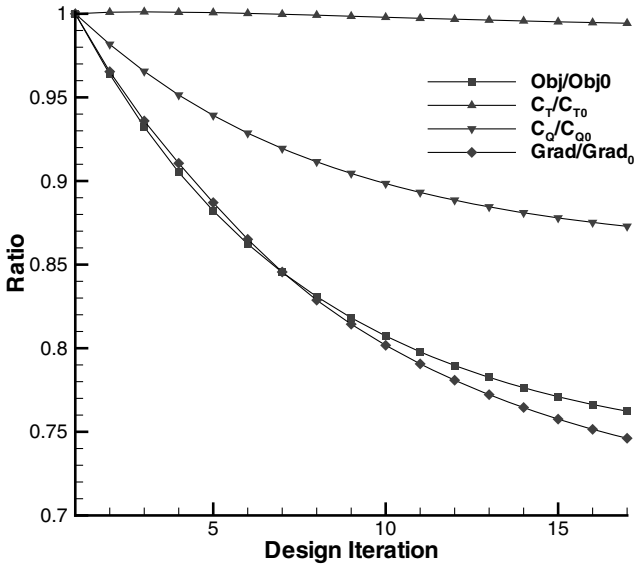

Fig. 13 Design convergence history of the UH-60 rotor blade.

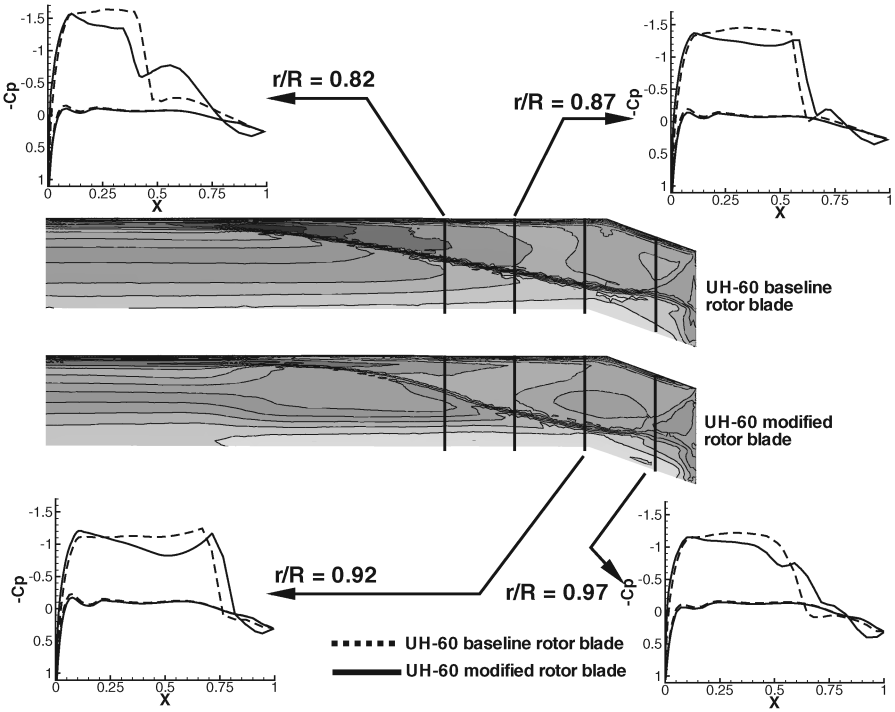

Fig. 14 Comparison of surface pressure distributions of the UH-60 rotor blade before and after design at a tip Mach number of 0.85 and a blade collective pitch angle of 10.47 deg.

In Fig. 5, the pressure contours on the blade upper surface and the sectional pressure distributions at four spanwise stations before and after the design optimization are compared. It shows that the shock wave on the original Caradonna–Tung rotor blade mostly disappeared at the inboard sections. At the outboard sections, even though the shock wave was not completely eliminated, the shock strength was greatly reduced after the design optimization.

In Fig. 6, the design convergence history of the Caradonna–Tung rotor blade is presented. It shows that the design process mostly converged after 25 design iterations. For the designed rotor, the required inviscid torque was reduced by approximately 15% from that of the original rotor due to the reduction of the shock strength and the wave drag while the loss in thrust was less than 4%. As a result, the inviscid figure of merit (a figure of merit based on surface pressures not including viscous skin friction) of the rotor increased by approximately 5.6% after the design. The total calculation time required for the optimization was approximately 4 h using 24 processors.

In Fig. 7, a comparison of the spanwise sectional thrust distributions of the rotor before and after the design is presented. It is observed that the loss in the total thrust mostly occured at the midspan, away from the transonic tip region where the present design optimization is most effective.

In Fig. 8, the blade section contours at four spanwise stations near the blade tip are compared between the original and designed rotors. It shows that the leading-edge radius and the blade thickness near the leading edge were slightly reduced at all design sections, inducing a slightly higher suction peak and helping to maintain the desired thrust. The blade thickness at the midchord increased, particularly at outboard sections accompanying the strong shock wave.

To check the off-design performance of the designed rotor blade, a flow calculation was made at a subsonic tip Mach number of 0.439 and a collective pitch angle of 8 deg. In Fig. 9, the surface pressure distributions of the blade before and after the design are presented. Unlike the transonic flow case, slight loss of the loading was observed near the leading edge due to the reduction of the blade thickness. However, some gain in the blade loading was also observed at the midchord because of the flow acceleration caused by the increased blade thickness. As a result, the total thrust obtained by the designed rotor blade was approximately 7% less than that of the original Caradonna–Tung rotor blade while the torque reduction was approximately 11%. The inviscid rotor figure of merit increased slightly by 1.6% after the design at this off-design operating condition.

UH-60 Rotor Blade

The second application of the present method was made to the optimal design of the UH-60 helicopter rotor blade. The UH-60 rotor has four twisted blades with an aspect ratio of 15.31, and the blades are composed of two sets of airfoil sections, SC1095 and SC1094R8. The blade planform has a backward sweep of 20 deg at the tip region [15].

Figure 10 shows the surface triangulations on the rotor blade. The computational domain was initially composed of 699,011 tetrahedral cells and 132,047 nodes. After applying three levels of solution-adaptive mesh refinement, the number of cells and nodes increased to 823,043 and 153,488, respectively. The mesh adaptation sequence is presented in Fig. 11. In the present calculation, the far-field boundary was set five radii away from the rotor in all directions.

Initially, validation of the present flow solver was made by calculating the aerodynamic loads of the rotor at a tip Mach number of 0.628 and a collective pitch angle of 10.47 deg. In Fig. 12, the surface pressure distributions at three spanwise stations of the blade are presented. It shows that comparison between the prediction made by the present unstructured adaptative mesh method and the experiment [15] is fair and the results are comparable to other predictions [15] based on an overset-grid Navier–Stokes method including blade elastic deflection.

Next, the aerodynamic shape optimization was applied to the UH-60 rotor blade at a transonic tip Mach number of 0.85, which is equivalent to the blade tip Mach number reached at the advancing side of the rotor in cruising forward flight. The collective pitch angle was set to 10.47 deg. Nine spanwise stations were selected as the design sections, mostly at the outboard end of the blade ($r/R = 0.65$, 0.70, 0.75, 0.80, 0.85, 0.90, 0.93, 0.95, 0.98), and 10 Hicks–Henne shape functions were adopted to represent the upper surface at each design section, resulting in 90 design variables in total.

In Fig. 13, the design history of the UH-60 rotor blade is presented. After 17 design iterations, the required inviscid torque was reduced

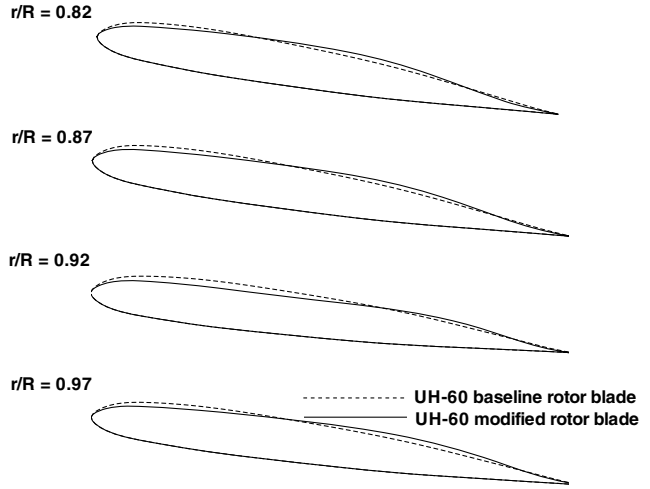

Fig. 15 Comparison of UH-60 blade section contours before and after design.

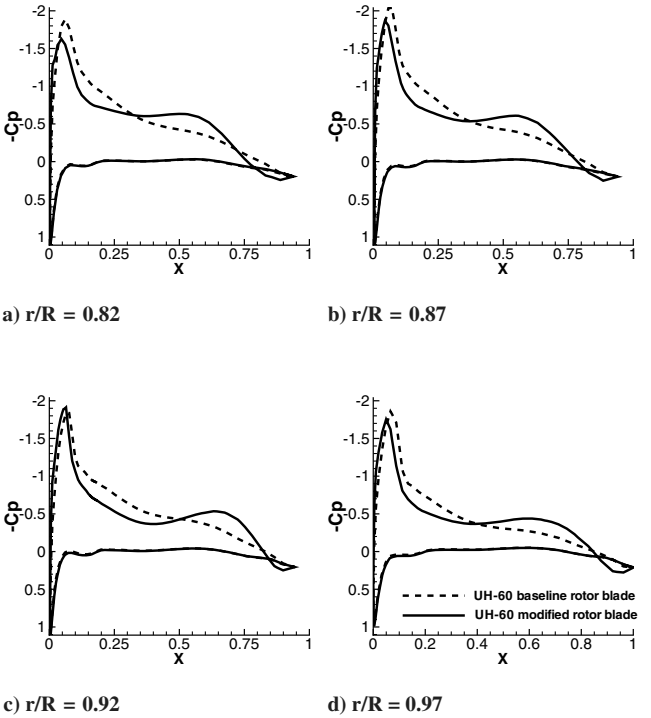

a) r/R = 0.82 **b) r/R = 0.87**

c) r/R = 0.92 **d) r/R = 0.97**

Fig. 16 Comparison of surface pressure distributions of the UH-60 rotor blade at an off-design subsonic tip Mach number of 0.628 and a blade collective pitch angle of 10.47 deg.

by 13% from the initial value while the thrust variation was less than 0.5%. As a result, the inviscid rotor figure of merit increased by 12.7% after the design optimization. The nose-up pitching moment was also reduced by 7.6% from that of the original rotor. The total calculation time required for the optimization was approximately 4.4 h using 24 processors.

In Fig. 14, the blade surface pressure contours and the sectional pressure distributions at four spanwise stations of the blade are compared before and after the shape optimization. It shows that the shock wave strength at the blade tip region was reduced, even though not completely eliminated, after the design optimization, resulting in the reduction of the required torque as shown in Fig. 13. The location of the shock wave moved further upstream, and the locally supersonic region was also reduced, particulary at the inboard sections.

In Fig. 15, the blade section contours at four selected spanwise stations are compared before and after the design optimization. It shows that the leading-edge radius and the blade thickness ahead of the midchord were slightly reduced for all design sections. Downstream of the midchord, the blade thickness was slightly increased, which is typical for inviscid section optimizations.

To check the rotor performance at an off-design condition, the flow calculation was made at a subsonic tip Mach number of 0.628 and a collective pitch angle of 10.47 deg, and the resultant surface pressure distributions are presented in Fig. 16. It shows that the aerodynamic loading was very much reduced ahead of the midchord while the loss was recovered downstream as a result of the thickness increase. The total thrust and torque obtained from the designed rotor blade at this off-design flight condition were 99.8% and 98.6% of those of the original rotor, respectively. The predicted inviscid rotor figure of merit at this off-design operating condition was 0.72 for the original UH-60 rotor, and the value did not change after the design. The measured figure of merit [15] was 0.73, and the predicted value based on a Navier–Stokes Method [15] was between 0.74 and 0.78. The nose-up pitching moment was also reduced by approximately 30% due to the increase of the aft loading.

Concluding Remarks

In the present study, an aerodynamic shape optimization technique has been developed for helicopter rotor blades in a transonic flow regime based on a continuous adjoint method on unstructured meshes. For this purpose, the flow solver and the adjoint sensitivity analysis were cast on the rotating frame of reference. The blade section contours were represented using the Hicks–Henne shape functions. A spring analogy technique was adopted to handle the mesh movement due to the change in the blade geometry. A parallel computation algorithm based on domain decomposition was also adopted for the efficient evaluation of the flow and adjoint solvers. A solution-adaptive mesh refinement technique was used to better resolve the tip vortex. The present method was applied to the Caradonna–Tung rotor blade and the UH-60 rotor blade for validation. It was demonstrated that the present aerodynamic shape optimization technique is effective and useful for the determination of optimum rotor blade configurations that require minimum inviscid torque while properly maintaining the desired thrust level at transonic flight conditions. Because reduction of induced power is also important for rotor blade design in hover, it is necessary to consider blade twist optimization simultaneously in future study.

References

[1] Jameson, A., and Vassberg, J. C., "Computational Fluid Dynamics for Aerodynamic Design: Its Current and Future Impact," AIAA Paper 2001-0538, 2001.

[2] Reuther, J. J., Jameson, A., Alonso, J. J., Rimlinger, M. J., and Saunders, D., "Constrained Multipoint Aerodynamic Shape Optimization Using an Adjoint Formulation and Parallel Computers, Part 1, 2," *Journal of Aircraft*, Vol. 36, No. 1, 1999, pp. 51–74.

[3] Kim, H. J., Obayashi, S., and Nakahashi, K., "Flap-Deflection Optimization for Transonic Cruise Performance Improvement of Supersonic Transport Wing," *Journal of Aircraft*, Vol. 38, No. 4, 2001, pp. 709–717.

[4] Elliott, J., and Peraire, J., "Practical 3D Aerodynamic Design and Optimization Using Unstructured Meshes," AIAA Paper 96-4170, 1996.

[5] Lee, S. W., and Kwon, O. J., "Parallel 3-D Aerodynamic Shape Optimization on Unstructured Meshes," *Korean Society for Aeronautical and Space Science International Journal*, Vol. 4, No. 1, 2003, pp. 45–52.

[6] Tapia, F., Sankar, L. N., and Schrage, D. P., "An Inverse Aerodynamic Design Method for Rotor Blades," *Journal of the American Helicopter Society*, Vol. 42, No. 4, 1997, pp. 321–326.

[7] Fanjoy, D. W., and Crossley, W. A., "Aerodynamic Shape Design for Rotor Airfoils via Genetic Algorithm," *Journal of the American Helicopter Society*, Vol. 43, No. 3, 1998, pp. 263–270.

[8] Sun, H., Kim, Y., Lee, S., and Lee, D., "Aerodynamic Design of Helicopter Rotor Blade in Forward Flight Using Response Surface Methodology," *Proceedings of the American Helicopter Society's 58th Annual Forum* [CD-ROM], American Helicopter Society, Alexandria, VA, 2002.

[9] Lee, S. W., and Kwon, O. J., "Aerodynamic Shape Optimization of Rotor Blades in Hover Using Unstructured Meshes," *Proceedings of the American Helicopter Society's 60th Annual Forum* [CD-ROM], American Helicopter Society, Alexandria, VA, 2004.

[10] Hicks, R. M., and Henne, P. A., "Wing Design by Numerical Optimization," *Journal of Aircraft*, Vol. 15, No. 7, 1978, pp. 407–412.

[11] Blom, F. J., "Consideration on the Spring Analogy," *International Journal for Numerical Methods in Fluids*, Vol. 32, No. 6, 2000, pp. 647–668.

[12] Kang, H. J., and Kwon, O. J., "Effect of Wake Adaptation on Rotor Hover Simulations Using Unstructured Meshes," *Journal of Aircraft*, Vol. 38, No. 5, 2001, pp. 868–877.

[13] Karypis, G., and Kumar, V., "Multilevel k-way Partitioning Scheme for Irregular Graphs," *Journal of Parallel and Distributed Computing*, Vol. 48, No. 1, 1998, pp. 96–129.

[14] Caradonna, F. X., and Tung, C., "Experimental and Analytical Studies of a Model Helicopter Rotor in Hover," NASA TM 81232, 1981.

[15] Ahmad, J. U., and Strawn, R. C., "Hovering Rotor and Wake Calculations with an Overset-Grid Navier-Stokes Solver," *Proceedings of the American Helicopter Society's 55th Annual Forum*, American Helicopter Society, Alexandria, VA, 1999, pp. 1949–1959.

[16] Frink, N. T., "Upwind Scheme for Solving the Euler Equations on Unstructured Tetrahedral Meshes," *AIAA Journal*, Vol. 30, No. 1, 1992, pp. 70–77.

[17] Srinivasan, G. R., Raghavan, V., and Duque, E. P. N., "Flowfield Analysis of Modern Helicopter Rotors in Hover by Navier-Stokes Method," *Journal of the American Helicopter Society*, Vol. 38, No. 3, 1993, pp. 3–13.

[18] Anderson, W. K., "Aerodynamic Design Optimization on Unstructured Grids with a Continuous Adjoint Formulation," AIAA Paper 97-0643, 1997.

[19] Strawn, R. C., and Barth, T. J., "A Finite-Volume Euler Solver for Computing Rotary-Wing Aerodynamics on Unstructured Meshes," *Journal of the American Helicopter Society*, Vol. 38, No. 2, 1993, pp. 61–67.

R. So
Associate Editor